High spatial range velocity measurements in a high Reynolds number turbulent boundary layer

C. M. de Silva,[1] E. P. Gnanamanickam,[1,2] C. Atkinson,[3] N. A. Buchmann,[3] N. Hutchins,[1] J. Soria,[3,4] and I. Marusic[1]
[1]*Department of Mechanical Engineering, University of Melbourne, Parkville, Victoria 3010, Australia*
[2]*Department of Aerospace Engineering, Embry-Riddle Aeronautical University, Daytona Beach, Florida 32114, USA*
[3]*Laboratory for Turbulence Research in Aerospace & Combustion, Monash University, Victoria 3800, Australia*
[4]*Department of Aeronautical Engineering, King Abdulaziz University, Jeddah, Kingdom of Saudi Arabia*

Here, we detail and analyse a multi-resolution particle image velocity measurement that resolves the wide range of scales prevalent in a zero pressure gradient turbulent boundary layer at high Reynolds numbers (up to $Re_\tau \approx 20\,000$). A unique configuration is utilised, where an array of eight high resolution cameras at two magnification levels are used simultaneously to obtain a large field of view, while still resolving the smaller scales prevalent in the flow. Additionally, a highly magnified field of view targeted at the near wall region is employed to capture the viscous sublayer and logarithmic region, with a spatial resolution of a few viscous length scales. Flow statistics from these measurements show good agreement with prior, well resolved hot-wire anemometry measurements. Analysis shows that the instantaneous wall shear stress can be reliably computed, which is historically known to be challenging in boundary layers. A statistical assessment of the wall shear stress shows good agreement with existing correlations, prior experimental and direct numerical simulation data, extending this view to much higher Reynolds numbers. Furthermore, conditional analysis using multiple magnification levels is detailed, to study near-wall events associated with high skin friction fluctuations and their associated overlaying structures in the log region. Results definitively show that the passage of very large-scale positive (or negative) velocity fluctuations are associated with increased (or reduced) small-scale variance in wall shear stress fluctuations.

I. INTRODUCTION

Fluid flows adjacent to a solid boundary (wall) are characterised by the presence of a boundary layer, involving very sharp velocity gradients. For the vast majority of flows in nature and engineering, the flows within these boundary layers are turbulent and are characterised by a hierarchy of length and time scales encapsulated within this thin region close to the wall. For recent reviews on the physics of wall-turbulence, readers are referred to Marusic *et al.*,[1] Klewicki,[2] and Jiménez[3] among others.

A characteristic number indicative of the range of length scales present within the turbulent boundary layer is the friction Reynolds number, or Kármán number, $Re_\tau = \delta^+ = \delta/(\nu/U_\tau)$ where U_τ is the friction velocity, δ is the boundary layer thickness, and ν is the kinematic viscosity. Re_τ is proportional to the ratio of the largest and smallest length scales in the flow. Consequently, the scale separation between the largest and smallest length scales increases with Re_τ. A vast number of examples of wall turbulence in engineering and nature occurs at high Re_τ, which include flows over aircrafts/ships ($\sim\mathcal{O}(10^5)$) and the atmospheric boundary layer ($\sim\mathcal{O}(10^6)$), to name a few.

Of specific interest to the flow physicist are the scales of turbulence prevalent in turbulent boundary layers. The scale-physics of high Re_τ turbulence is reviewed in some detail by Smits, McKeon, and Marusic.[4] To summarise, at low to moderate Re_τ ($\lesssim 5000$) much of the turbulent energy production occurs in the near wall region and the associated smaller scales ($\mathcal{O}(10-100)\nu/U_\tau$). As Re_τ increases the larger scales ($\mathcal{O}(10^3\nu/U_\tau)$ to $\mathcal{O}(\delta)$) much farther from the wall are responsible for an increasing magnitude of turbulent energy production,[5] eventually surpassing the near-wall cycle at sufficiently high Re_τ. In addition, within the entire boundary layer the turbulent energy is dissipated on the order of the Kolmogorov length scale η, which increases marginally from about two viscous units in the near-wall region to approximately 20 viscous units in the outer region (at $Re_\tau \approx \mathcal{O}(10^4)$).

The inhomogeneous nature of wall turbulence lends itself to the characterisation of the turbulence into structures, eddies, or coherent motions (and their associated scales, statistics, and interactions) with the long-term goal of developing turbulence models with a predictive capability.[6] For a detailed overview of the current viewpoints on eddies, structures, and coherent motions in wall turbulence, along with the associated literature, readers are directed towards recent summaries by Marusic and Adrian[6] and Herpin *et al.*[7] A variety of different coherent motions have been observed within the boundary layer including stream-wise vortices, ejection and sweeps, hairpin vortices (and packets), low and high-speed streaks, large three-dimensional bulges and superstructures. From a scale perspective, the inherent hierarchy of scales within a turbulent boundary layer manifests itself in these coherent motions, which range from a few tens of viscous units (core diameters of near-wall stream-wise vortices) to several δ (streamwise extent of superstructures in the outer region).[8]

Both experimental and Direct Numerical Simulation (DNS) studies of turbulent boundary layers, at high Re_τ, present major challenges due to the large range of length scales that need to be resolved. Measurements or computational studies at high Re_τ to study the interaction of a range of scales should at the very least, have sufficient spatial resolution to resolve the smaller coherent motions across the entire boundary layer ($\mathcal{O}(10\eta)$), while also having the necessary spatial domain to capture the larger structures ($\mathcal{O}(\delta)$). Indeed, since the largest structures extend to several δ in the streamwise direction, the spatial domain in this direction should be as large as possible. At the Reynolds numbers considered in this study ($Re_\tau \approx 8000$–$20\,000$), this requirement necessitates nearly four orders of magnitude of length scales to be measured simultaneously to capture this full range of scales. DNS databases at moderate Re_τ (for example, channel flow DNS databases up to $Re_\tau \approx 2000$ by Hoyas and Jimenez[9] and spatially developing turbulent boundary layers DNS databases up to $Re_\tau \approx 4000$ by Pirozzoli and Bernardini[10] and $Re_\tau \approx 1270$ by Schlatter and Örlü[11]) provide unprecedented three-dimensional details of the flow field that cannot be experimentally matched primarily due to the resolution, dimensional, and technological limits of measurement techniques. However, the current memory and computational limitations make experimental analysis of high Re_τ flows more feasible than DNS studies. Hence, overcoming measurement challenges in high Re_τ facilities is essential, since such measurements provide an opportunity to bridge the gap between DNS datasets and practical engineering applications. With this goal in mind, a particle image velocimetry (PIV) based technique, is used to carry out high resolution measurements in a high Re_τ turbulent boundary layer.

PIV has become increasingly popular over the last decade for carrying out accurate measurements of multi-component, multi-dimensional, large field of view (FOV) velocity fields in turbulent flows. For excellent reviews of PIV based techniques, readers are directed to Raffel *et al.*[12] and Adrian and Westerweel.[13] One early attempt to apply PIV in turbulent boundary layers, with a high dynamic spatial range, is the experimental work carried out by Adrian, Meinhart, and Tomkins.[14] These experiments were conducted at relatively moderate Re_τ (up to $Re_\tau \approx 2000$), but had a uniquely large range of scales that was resolved simultaneously (in excess of 200:1). The spatial signature and organisation of flow structures visualised in this study would not have been possible without simultaneously resolving both large and small length scales. Adrian, Meinhart, and Tomkins[14] used a 4×5 in. photographic film to capture a field of view in excess of δ in both the streamwise and wall-normal directions. The use of photographic film provided images that could subsequently be digitised to a very high resolution, allowing small length scales of the order of $\sim 3-5\eta$ to be resolved, but still having a spatial domain of over δ. However, this was at the tradeoff of capturing

a few realisations due to the tedious process involved in developing photographic film. Moreover, the flow structures in the near-wall region ($<100\nu/U_\tau$) were not resolved using this measurement scheme due to glare from the wall. Nevertheless, the dataset provides a substantial contribution to understanding the structural framework of turbulent boundary layers, and to date has one of the largest dynamic spatial ranges for a PIV based measurement.[15]

Following from the work of Adrian, Meinhart, and Tomkins,[14] PIV based measurements in turbulent boundary layers have been advanced by considering different measurement plane orientations, or measurement techniques. These include Herpin *et al.*,[7] Tomkins and Adrian,[16] Hutchins, Hambleton, and Marusic,[17] Carlier and Stanislas,[18] Hambleton, Hutchins, and Marusic,[19] Lin *et al.*,[20] Herpin *et al.*,[21] to name a few. More recently volumetric PIV measurements have also been carried out by Schröder *et al.*,[22] Elsinga *et al.*,[23,24] and Clark.[25] However, one should note that the dynamic velocity and spatial range of most of these datasets are lower than those achieved by Adrian, Meinhart, and Tomkins[14] as summarised in Westerweel, Elsinga, and Adrian.[15] Concurrent to the acquisition of several experimental datasets, substantial progress in advanced PIV algorithms and novel experimental configurations have been made in recent years. One such experimental framework is the use of multiple FOVs at different magnification levels by Cierpka, Scharnowski, and Kähler.[26] A higher magnification was employed for the FOV closest to the wall to capture the smaller length scales. Meanwhile, the FOV closer to the free stream had a lower magnification to capture the larger length scales. However, each magnification level was acquired independently, thus precluding a complete instantaneous snapshot of the entire boundary layer.

A decade after the work of Adrian, Meinhart, and Tomkins,[14] we now present measurements at high Re_τ that increases the simultaneously resolved spatial range by over an order of magnitude, while capturing over 1500 realisations, to compute converged statistics. Such advancements have been made possible by the implementation of a unique measurement configuration (similar to that of Cierpka, Scharnowski, and Kähler[26]) in a large-scale facility, complemented by improvements in camera resolution and post-processing algorithms. Following Cierpka, Scharnowski, and Kähler,[26] a hierarchy of magnifications (nested within each other) captured simultaneously is adopted in this paper to provide instantaneous snapshots of the entire boundary layer, with a field of view extending for several δ in the streamwise direction, yet still with sufficient resolution to resolve scales of a few η. The novelty of the datasets presented lies in the use of a total of nine cameras at three magnification levels, simultaneously. This paper describes in detail the experimental setup, which includes camera and laser orientation, timing, and calibration. Flow statistics of the boundary layer at three Reynolds numbers are presented and compared to established correlations. A snapshot of the velocity field in the boundary layer and conditional velocity fields are used to illustrate the uniqueness of the present dataset. Probability density functions (pdf's) of the wall shear stress, estimated using the measured near-wall velocity are also presented.

Throughout this paper the coordinate system x, y, and z refers to the streamwise, spanwise, and wall-normal directions, respectively. The instantaneous streamwise and wall-normal velocities are represented by $\widetilde{U}$ and $\widetilde{W}$, respectively, with the corresponding velocity fluctuations given by u and w. Capitalisation and overbars indicate averaged quantities, and the superscript $+$ refers to normalisation by viscous scales. For example, we use $l^+ = lU_\tau/\nu$ for length and $U^+ = U/U_\tau$ for velocity, where U_τ is the friction velocity and ν is the kinematic viscosity of the fluid.

II. EXPERIMENTAL SETUP

The experiments are performed in the High Reynolds Number Boundary Layer Wind Tunnel (HRNBLWT) at the University of Melbourne. The test section of the facility has a development length of approximately 27 m, offering the capability of achieving high Re_τ at relatively low freestream velocities. This results in a larger viscous length scale and hence less acute spatial resolution issues. Further details of the facility and flow quality are provided in Nickels *et al.*[27] Figure 1 shows a schematic of the measurement station which is located 21 m downstream of the trip. Measurements are conducted at three freestream velocities (10, 20, and 30 ms^{-1}), with corresponding Reynolds numbers based on friction velocity of $Re_\tau \approx 8000$, 14 500, and 19 500, respectively. Additional flow parameters are summarised in Table I.

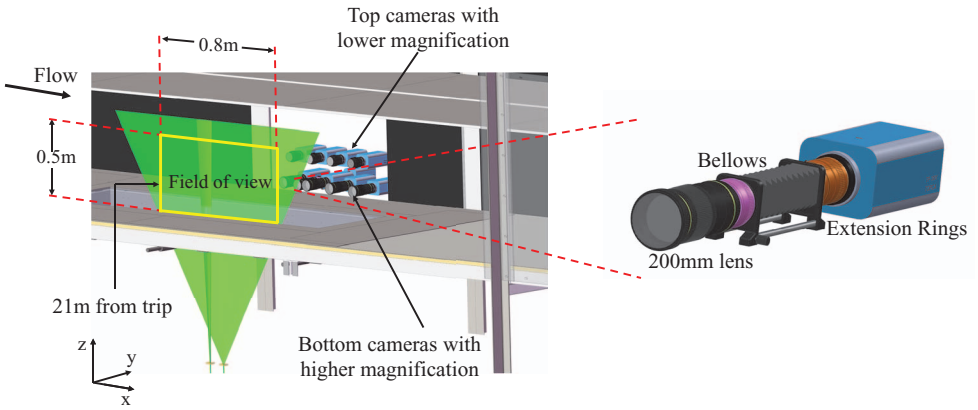

FIG. 1. Experimental setup used to conduct planar PIV experiments in the HRNBLWT. (Left) The camera setup in the facility to obtain the large field of view (FOV), simultaneously with the high-mag FOV using a second laser sheet and high magnification optics on a ninth camera. (Right) A scaled schematic of high magnification camera H_1.

The entire FOV is divided into a large FOV and an independent highly magnified (high-mag) FOV, for imaging purposes. The velocity field from the large FOV spans 0.8 m × 0.5 m, and is captured by eight PCO4000 cameras (4008 × 2672 pixels each). This unique eight camera configuration is arranged in two rows, with four cameras in each row as shown in Figure 2. The four cameras on the top row (T_{1-4}) are at a lower magnification than the four cameras on the bottom row (B_{1-4}). The differing magnification accounts for the reduction in size of the most prevalent coherent structures and their organisation closer to the wall. Figure 2 also demarcates the FOV imaged by each of the nine cameras (indicated by dashed lines), which are overlaid on colour contours of instantaneous streamwise velocity. Shaded contour colours indicate the streamwise velocity magnitude at a freestream velocity of $U_\infty = 10$ ms^{-1}. Furthermore, in order to capture the finer scales closest to the wall and the instantaneous wall shear stress, a ninth camera, H_1 (referred to as high-mag) is fitted with high magnification optics. This high-mag FOV is nested within the larger FOV as shown in Figure 2, imaging an area of approximately 750 × 500 wall units (in the streamwise and wall-normal directions).

A. Illumination

The particles are illuminated by two laser sheets overlapping in the spanwise direction. These sheets are generated using two Spectra Physics "Quanta-Ray" PIV 400 Nd:YAG double-pulse lasers that deliver 400 mJ/pulse each. One laser-pair is dedicated to illuminate the large FOV, and the second laser-pair is used to illuminate the high-mag FOV in the near wall region. The necessity of a large amount of concentrated power for the high-mag FOV is primarily due to the loss of light through the optical configuration (shown in Figure 1), where the object distance from the sensor is ≈1 m and yet the high-mag FOV spans just ≈ 0.03 m × 0.02 m in x and z, respectively. A bellows, tele-converter, and a series of extension tubes are used to obtain the necessary magnification rather than employing a long-range microscope.[26] This approach is adopted due to the large sensor size of

TABLE I. Flow parameters for the three PIV datasets.

Re_τ	Re_δ	Re_θ	U_∞ [ms^{-1}]	U_τ [ms^{-1}]	δ [m]	ν/U_τ [μm]	# Images
8000	2.4×10^5	22 400	10	0.334	0.36	45	1680
14 500	4.6×10^5	40 800	20	0.630	0.35	24	1680
19 500	6.3×10^5	54 000	30	0.935	0.34	17	1680

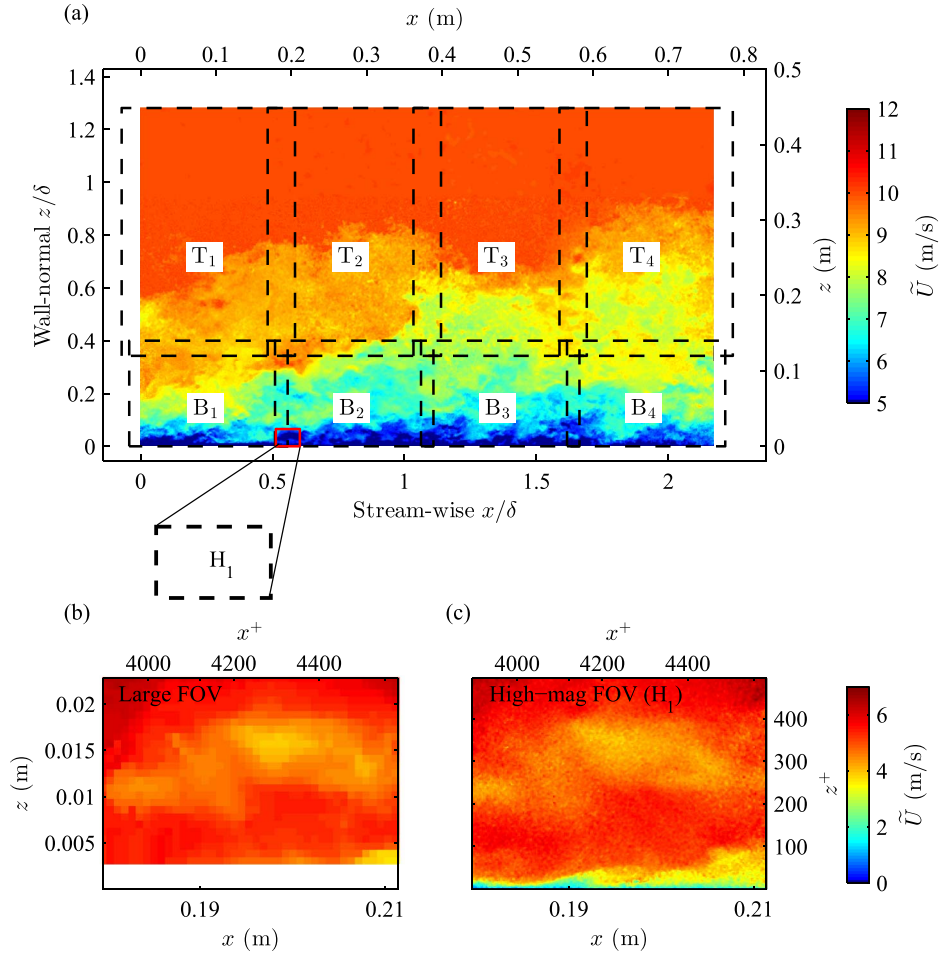

FIG. 2. (a) Instantaneous streamwise velocity across the FOV of the eight cameras (B_{1-4} and T_{1-4}), H_1 indicates the location of the high-mag FOV nested within the larger FOV in the near wall region. The location $x = 0$ is located 21 m downstream of the trip. (b) Instantaneous streamwise velocity seen by the large FOV in the region captured by the high-mag FOV (H_1). (c) Region in (b) as seen with the high magnification camera.

the camera utilised, enabling the full use of the sensor and resolution of the camera, but at the cost of a significant drop in intensity level.

B. Experimental parameters

The use of multiple laser pairs to illuminate FOVs with varying magnifications leads to different intensity levels between them, causing experimental challenges that are addressed as follows. First, due to the significantly higher intensity of the high-mag FOV laser sheet, it is triggered a few microseconds prior to the large FOV laser sheet. This avoids saturation of the large FOV cameras. Figure 3 illustrates the timing between the two laser pairs and the two sets of cameras (large FOV and high-mag FOV) at $U_\infty = 10\,\mathrm{ms}^{-1}$. The abscissa shows the offset (in microseconds) between the laser pairs, and the camera triggers for the large FOV and high-mag cameras. The effective offset between the large FOV and high-mag FOV velocity fields is 60 μs, which corresponds to $\approx$0.5 viscous time units ($t^+ = tU_\tau^2/\nu$). Therefore, it is reasonable to assume Taylor's hypothesis (the turbulence is frozen within this offset). Since the effective offset between the velocity fields is known, it is easily accounted for while stitching the images together. A similar offset (in terms of viscous time scale) is used while carrying out measurements at freestream velocities of $U_\infty = 20\,\mathrm{ms}^{-1}$ and $U_\infty = 30\,\mathrm{ms}^{-1}$. It should be noted that the high-mag camera is exposed when

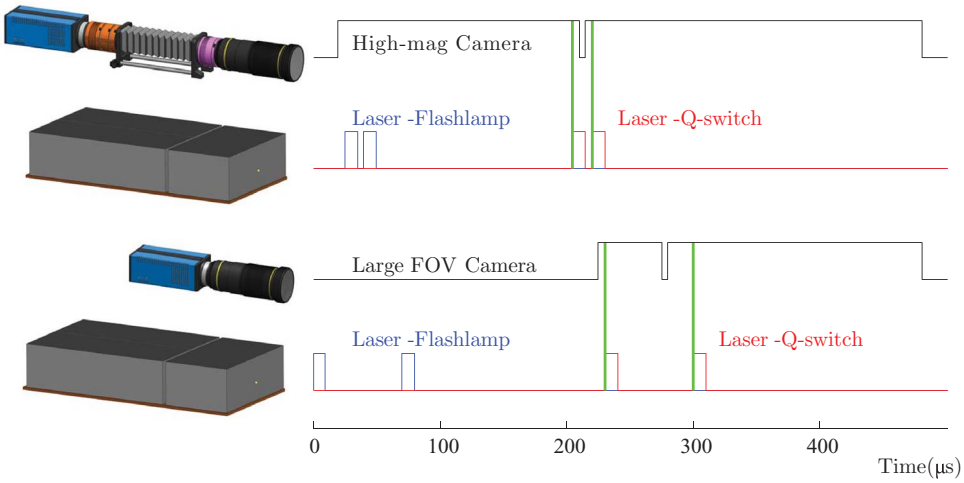

FIG. 3. Schematic of the timing between the cameras and laser pairs at $U_\infty = 10\,\mathrm{ms}^{-1}$. The high magnification images are taken prior to the large FOV with a small offset in time to avoid overlap. The green vertical lines correspond to when each laser fires.

the laser pair for the large FOV is fired. However, due to the significant loss of light in the optical configuration of the high-mag camera, the intensity level of the large FOV laser pair as seen by the high-mag camera is below background noise levels, and is easily removed during image pre-processing.

Table II summarises the experimental parameters of the present study. Optimal parameters for the experiment such as particle size, density, and displacement cannot be adapted for each magnification level simultaneously. Rather, parameters are chosen to obtain reasonable accuracy at all magnification levels. Seeding is introduced into the whole laboratory to obtain a homogeneous seeding density across the test section. Additional seeding is also injected into the near wall region, in close proximity to the blower fan, but prior to the flow conditioning of the facility (to minimise any impact on the flow within the working section). This is necessary to account for the lower seeding concentration typically observed in the near wall region, which becomes more pronounced in the high-mag FOV. Since the high-mag FOV is illuminated using an independent laser pair the particle displacement captured by it is optimised independently. Conversely, the two magnifications used

TABLE II. Experimental parameters for the nested multi-resolution PIV experiments.

Large FOV	
Field of view	$\approx$0.8 m $\times$ 0.5 m
Depth of field	$\approx$2 mm
Optical magnification	$\approx$55 μm/pixel (B_{1-4}) and $\approx$90 μm/pixel (T_{1-4})
Number of velocity vectors per image	$\approx 1.5 \times 10^6$
Laser sheet thickness	$\approx$0.5 mm (11^+ at $Re_\tau \approx 8000$)
High-mag FOV	
Field of view	$\approx$30 mm $\times$ 20 mm
Depth of field	$\approx$0.3 mm
Optical magnification	$\approx$7.5 μm/pixel
Number of velocity vectors per image	$\approx 4 \times 10^4$
Laser sheet thickness	$\approx$0.5 mm (11^+ at $Re_\tau \approx 8000$)
Particle size	$\approx$1 μm
Seeding	Polyamide particles
Flow medium	Air

for the large FOV are illuminated using a single laser pair. Therefore, the particle displacements are optimised by considering the two magnification levels simultaneously.

C. Calibration

Planar PIV measurements are typically calibrated using a pixel to real space conversion based on a scaling factor, determined by an *in situ* calibration. This is simply performed by the imaging of an appropriate scale. However, planar PIV images are also typically affected by perspective and optical distortion from the optics, particularly when the FOV is large and misalignments often exist between the image plane and laser sheet.[13] To account for this, a large calibration grid which spans the length of the large FOV is imaged. The calibration grid is used to determine calibration coefficients which map each camera's pixel space (X, Z) to real space (x, z), and enables one to stitch the velocity fields from multiple cameras. The calibration grid used for the large FOV has a grid spacing of 5 mm. Meanwhile, for the high mag FOV which spans only a few centimeters in width, a smaller grid spacing of 2 mm is employed.

Precisely locating the wall position is a key issue for most PIV measurements in wall-bounded flows. This is particularly true when considering a streamwise wall-normal plane due to wall reflections caused by the laser sheet.[13] Here, to ascertain the wall location, we utilise the reflection of the calibration grid on the glass wall. It should be noted that there can be very small errors in relation to the positioning of the calibration target and imperfections on the glass wall. However, mean flow statistics presented in the subsequent analysis indicate that this error is less than $\sim$1 wall unit.

D. Processing

The experimental data are processed using an in-house PIV package, similar to that used in de Silva *et al.*[28,29] Interrogation windows of various sizes (ranging from 16 × 16 to 32 × 32 pixels) are used at each magnification level and are summarised in Table III. In order to minimise the variation in spatial resolution between the Re_τ studied, the interrogation window sizes are reduced for the high Re_τ datasets when possible as summarised on Table III. To maintain uniform vector spacing across the large FOV, the vector grid in real space is determined with an overlap of 50% for the bottom cameras. The vector spacing for the top cameras is then matched with the spacing of the bottom cameras. A mapping to real space from pixel space is established via the calibration procedure, detailed previously. The high-mag FOV has a pixel size of approximately 7.5 μm square, which is equivalent to 0.16 viscous length scales at $Re_\tau = 8000$. Therefore, an interrogation window size of 32 × 32 pixels is maintained across all Re_τ considered. This corresponds to approximately 5 × 5 and 14 × 14 wall units at $Re_\tau = 8000$ and $Re_\tau = 19\,500$, respectively, and a corresponding vector spacing of 2.5 and 7 wall units (at 50% overlap).

The average particle size in the image plane varies between the three magnifications, and a certain degree of peak (pixel) locking is observed in the large FOV velocity field due to the lower magnification, which leads to a lower particle image diameter. To account for pixel locking, a correction detailed in Roth and Katz[30] is used to treat the initial pixel locked PIV velocity field.

TABLE III. Summary of processing parameters of the experimental data. The interrogation window sizes used in this analysis are given in viscous units (l^+) and pixels.

			Interrogation window size					
			Bottom camera		Top camera		High-mag	
U_∞ (m/s)	Re_τ	ν/U_τ (μm)	l^+	pixels	l^+	pixels	l^+	pixels
10	8000	45	39	32 × 32	64	32 × 32	5	32 × 32
20	14 500	24	37	16 × 16	90	24 × 24	10	32 × 32
30	19 500	17	52	16 × 16	127	24 × 24	14	32 × 32

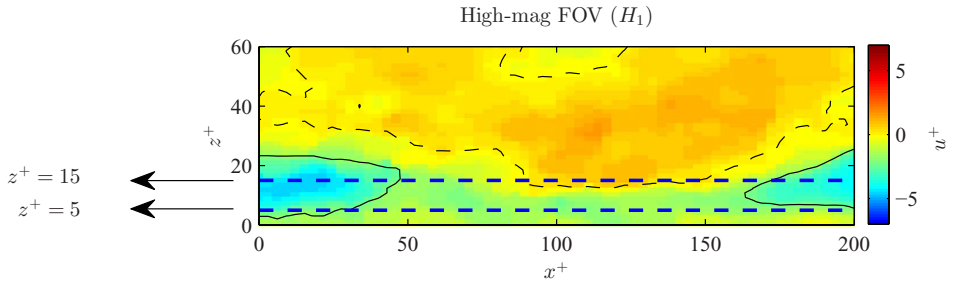

FIG. 4. Colour contours of instantaneous streamwise velocity fluctuations obtained from the high magnification camera in the near wall region. The horizontal dashed lines indicate the end of the viscous sublayer ($z^+ = 5$) and the location of the inner peak in the streamwise turbulence intensity ($z^+ = 15$). The solid and dashed contour lines are drawn at a levels of -2 and 0, respectively.

III. SPATIAL RESOLUTION

The uniqueness of the measurements detailed lies in the range of magnifications employed simultaneously to resolve the cascade of length scales present in a high Reynolds number turbulent boundary layer. Figure 2(a) gives a good visual representation of the range of length scales associated with a typical high Reynolds number flow. Figure 2(b) shows the region of the large FOV which is simultaneously captured by the high-mag FOV camera (shown in Figure 2(c)). Comparisons between Figures 2(b) and 2(c) clearly show the loss of small scale information in the large FOV. In addition, the lack of reliable data below $z^+ < 75$ in the wall normal direction for the large FOV is also evident, which is highlighted in the flow statistics shown in a subsequent section. Meanwhile, the high-mag FOV resolves much finer scales with reliable velocity vectors significantly closer to wall. Finally, a large scale correlation between the high-mag FOV and the large FOV is observed between Figures 2(b) and 2(c), thus demonstrating the capability for synchronous capture of both FOVs.

The high-mag FOV camera employed in this study provides reliable instantaneous velocity vectors in close proximity to the wall, well within the viscous sublayer ($z^+ < 5$). Figure 4 shows an example of the instantaneous streamwise velocity fluctuations obtained from the high-mag FOV, which indicates qualitatively that the instantaneous velocity field within the viscous sublayer is captured by the high-mag FOV. Previous hot-wire measurements carried out in the same facility and most other measurements at an equivalent Re_τ have failed to capture a well resolved velocity signal within the viscous sublayer. Therefore, results presented here are among the first well resolved spatial velocity measurements within the viscous sublayer in a zero pressure gradient turbulent boundary layer at $Re_\tau \approx \mathcal{O}(10^4)$.

Adrian and Westerweel[13] proposed the dynamic velocity range (DVR) and dynamic spatial range (DSR) as indicative measures to assess the ability of PIV measurements to measure spatial and temporal variations in the flow. Here, DVR is defined as the ratio of the maximum velocity to the minimum resolvable velocity, and is given by

$$\mathrm{DVR} = \frac{\Delta x_{max}}{c_\tau d_\tau}, \tag{1}$$

where Δx_{max} is the full-scale displacement, and c_τ is a constant that depends on the ability of the analysis procedure to determine the displacement between the images, and d_τ corresponds to the particle diameter on the image.[31] Similarly, DSR equals the ratio of the maximum resolvable length scale and is defined as

$$\mathrm{DSR} = \frac{L_x}{\Delta x_{max}}, \tag{2}$$

where L_x is the linear dimension of the FOV. These two quantities are used to compute a dimensionless constant DVR $\times$ DSR defined as

$$\mathrm{DVR} \times \mathrm{DSR} = \frac{L_x}{c_\tau d_\tau}, \tag{3}$$

TABLE IV. The dynamic spatial range (DSR) and dynamic velocity range (DVR) for the datasets from the present study and Adrian, Meinhart, and Tomkins,[14] a conservative estimate of $c_\tau = 0.1$ is used in Eq. (3).

	Re_τ	DSR	DVR	DVR × DSR
Adrian, Meinhart, and Tomkins[14]	876	270	90	25 000
Large FOV (present study)	8000–19 500	1500	80	120 000
High-mag FOV (present study)	8000–19 500	350	60	20 000

which is characteristic to each PIV system.[31] Westerweel, Elsinga, and Adrian[15] uses the parameter DVR × DSR in a recent review to quantify the performance of several measurements. For example, measurements by Adrian, Meinhart, and Tomkins[14] had a DVR × DSR ≈ 25 000, which is considered to be one of the highest DVR × DSR for PIV measurements to date.[15]

In the present study, the large FOV and high-mag FOV operate at a DVR × DSR ≈ 120 000 and 20 000, respectively (summarised in Table IV). We note that in a recent review by Westerweel, Elsinga, and Adrian[15] a DSR of at least $\mathcal{O}(10^3)$ is suggested, to resolve a large proportion of the coherent motions at $Re_\tau \approx \mathcal{O}(10^4)$, which is achieved in this study. Hence, this enables us to quantitatively analyse a wide spectrum of coherent structures. This includes scales from $\mathcal{O}(z^+)$ to large scale motions (LSM) of $\mathcal{O}(\delta)$ using the large FOV, only leaving the largest of structures (superstructures) unreachable. Furthermore, the high-mag FOV, resolves the most prevalent structures in the near-wall and log region while also resolving the instantaneous wall shear stress. This allows the investigation of near wall events and their links with larger features that populate the log and wake regions.

The spatial resolution of the measurement can also be assessed against the Kolmogorov length-scale of the flow to be studied. Figure 5 shows how the inner-scaled Kolmogorov length-scale (η^+) varies across the boundary layer for a range of Reynolds numbers. These estimates of η are obtained from single component hot-wire anemometry measurements from Hutchins *et al.*[32] and use the assumption of local isotropy, where the turbulent dissipation rate (ϵ) is approximated using $15\nu\overline{(\partial u/\partial x)^2}$. The horizontal lines correspond to the spatial resolution of the high-mag and large FOV at the lowest and highest Re_τ in this study. Here, we observe that the high-mag FOV has sufficient spatial resolution to resolve features in the order of η (indicative of the smallest scales of turbulence in the flow), meanwhile although the spatial resolution of the large FOV is over an order

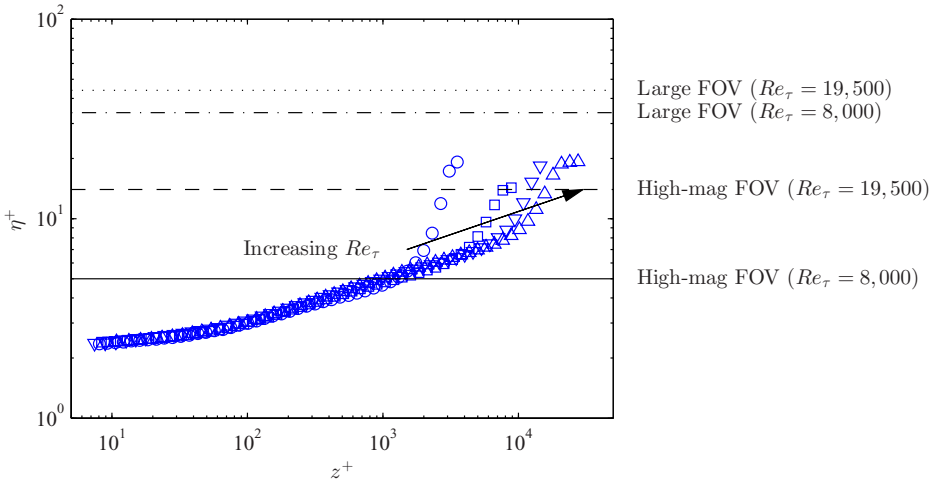

FIG. 5. Inner-scaled Kolmogorov length-scales (η^+) from hot-wire anemometry measurements.[32] The ○, □, ▽, and △ correspond to Re_τ of 2800, 7300, 13 600, and 19 030, respectively. The solid and dashed lines correspond to the spatial resolution of the high-mag FOV at $Re_\tau \approx 8000$ and ≈19 500, respectively. Similarly, the horizontal dashed-dotted and dotted lines correspond to the spatial resolution of the large FOV at $Re_\tau \approx 8000$ and ≈19 500, respectively.

of magnitude larger than η it is still sufficient to resolve most of the coherent motions within the turbulent boundary layer.

IV. RESULTS

A. Flow statistics

The realization of over 1500 instantaneous velocity snapshots at each Re_τ studied allows for the calculation of well converged velocity statistics and subsequent comparison with corresponding hot-wire measurements and DNS datasets. This enables us to quantify the accuracy of the measurements performed, and to establish the consequences of using three levels of magnification simultaneously. Mean flow (U^+) and turbulence intensity ($\overline{u^2}^+$) profiles are compared with hot-wire anemometry measurements at a matched Reynolds number in the same facility from Kulandaivelu.[33]

Figures 6(a) and 6(b) show a comparison of streamwise mean velocity and turbulence intensity profiles from this study (— and • correspond to the large and high-mag FOV, respectively) against well resolved hot-wire measurements (○) at $Re_\tau \approx 8000$ from Kulandaivelu.[33] It should be noted that all profiles from this study are normalised using U_τ determined using the near-wall gradient acquired from the high-mag FOV. The vertical dashed line represents the demarcation between the bottom (B_{1-4}) and top (T_{1-4}) cameras of the large FOV. Figure 6(a) shows that the large FOV yields

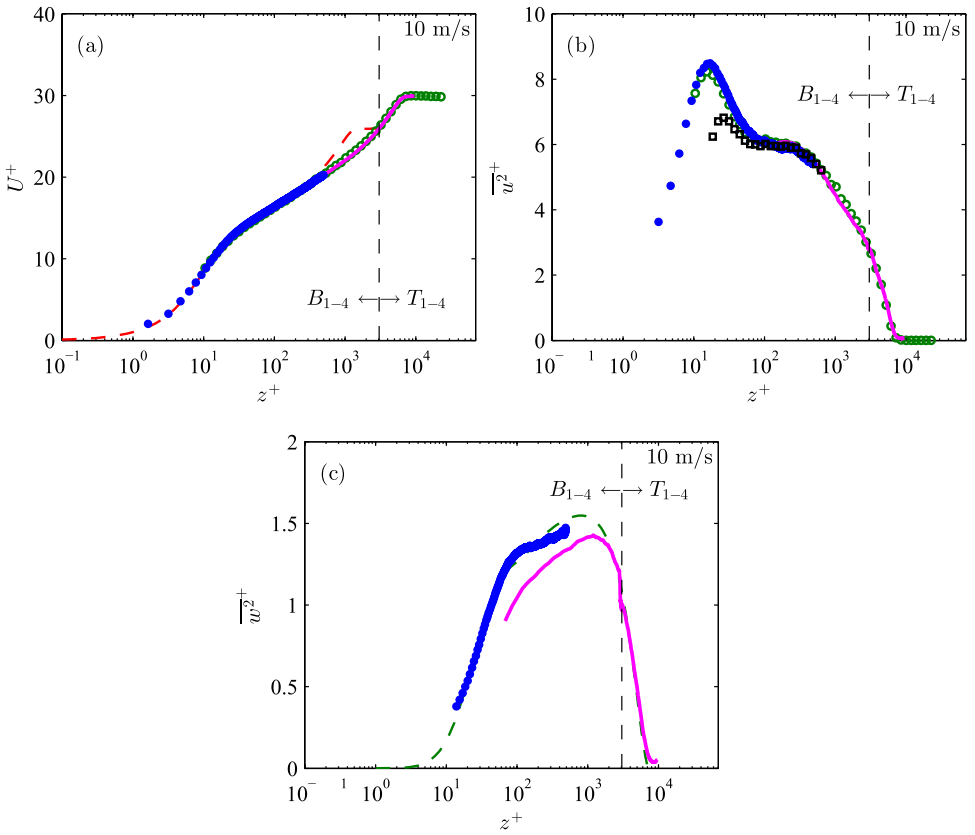

FIG. 6. Comparison of planar PIV, hot-wire anemometry experiments and empirical formulations at $Re_\tau \approx 8000$ for flow statistics (a) U^+, (b) $\overline{u^2}^+$, and (c) $\overline{w^2}^+$. The green ○ symbols represent the hot-wire data, the solid magenta line (—) indicates the large FOV PIV (present study), and the blue • symbols correspond to the high-mag PIV (present study). The dashed red line (−−) for U^+ is from direct numerical simulation data at $Re_\tau = 1270$ from Schlatter and Örlü,[11] and the dashed green (−−) line in (c) is a predicted profile from an empirical formulation at an equivalent Reynolds number.[34] The black □ symbols show a estimated profile ($\overline{u_f^2}^+$) at a matched spatial resolution to the large FOV. The vertical dashed line represents the demarcation between the bottom (B_{1-4}) and top (T_{1-4}) cameras in the large FOV.

accurate mean streamwise velocity measurements for $z^+ > 100$, meanwhile the high-mag FOV extends this range to within a few wall units $(1 - 3)$ from the wall. We note a clear peak is observed in the streamwise turbulence intensity profile ($\overline{u^2}^+$) at $z^+ = 15$ from the high-mag FOV (rarely captured by PIV measurements at high Re_τ). There is a slight difference (approximately 3%) in the magnitude of this peak between the current PIV experiments and the hot-wire data, with the PIV data returning the higher result. This discrepancy is within the relative measurement errors of these two techniques. However, it is also noted that these two measurements have very different spatial resolutions. The hot wire data of Kulandaivelu[33] is spatially averaged over 22 viscous units in the spanwise direction only (one-dimensional averaging), while the high-mag PIV is averaged over an interrogation volume of $5 \times 5 \times 6$ viscous units. We can quantify this difference in spatial averaging by using the DNS database of Hoyas and Jimenez.[9] The fluctuating velocity fields from this DNS database are filtered at the two appropriate scales. The high-mag PIV resolution is simulated by convolving the fluctuating velocity field with a top-hat filter function at $5 \times 5 \times 6$ viscous units. Meanwhile, the hot-wire resolution is simulated by averaging over 22 viscous units in the spanwise direction. This analysis shows that the attenuation due to a spatial averaging volume of $5 \times 5 \times 6$ viscous units is less than that due to one-dimensional averaging in the spanwise direction at 22 wall units, reaffirming the trends shown in Figure 6(b).

We might expect the influence of spatial averaging to be more pronounced for the large FOV due to the significantly larger viscous scaled interrogation window size. However, this is not noticeable in the large FOV turbulence intensity profile (shown in Fig. 6(b)), primarily because the near wall region, where spatial averaging is most acute due to the dominance of smaller length scales, is not captured. To illustrate this, we use the turbulent channel flow DNS database[9] spatially box filtered at $39 \times 39 \times 11$ viscous units to compute a filtered streamwise turbulence intensity profile at a spatial resolution matched to the large FOV PIV. We also filtered the data in the spanwise direction only with a filter length of 22 viscous units to simulate the spatial resolution of the hot-wire measurement. By calculating the difference between these two filtered views ($\overline{u^2}_d^+$), we are able to predict the missing energy owing to a volume averaging as compared to the one-dimensional averaging of a hot-wire, albeit for a channel flow at $Re_\tau = 934$.

As detailed in Hutchins *et al.*[32] the influence of spatial averaging is most prevalent when considering contributions to $\overline{u^2}^+$ from smaller length scales and shows minimal variation with increasing Re_τ. Furthermore, it is well documented that the near wall energy content shows good similarity between channel flows and turbulent boundary layers.[35] Equipped with this knowledge we can attempt to estimate the PIV measured variance (accounting for spatial averaging) in a turbulent boundary layer at high Re_τ, by subtracting the difference ($\overline{u^2}_d^+$) from a hot-wire measurement at an equivalent Re_τ. This predicted filtered result $\overline{u_f^2}^+$ (shown with black □ symbols on Figure 6(b)) confirms that the influence of the spatial averaging is most prevalent below $z^+ = 100$. This region is not captured by the large FOV, which may explain the agreement between the large FOV and the well-resolved hot-wire measurement.

We should also note that PIV measured variances are subject to two competing errors. Spatial resolution will tend to attenuate the magnitude of fluctuations, reducing the measured variance. However, PIV results are also subject to measurement noise which tends to offset this attenuation, artificially increasing fluctuations (see Atkinson *et al.*[36] for a detailed discussion of this).

If we consider the wall-normal turbulence intensity profile ($\overline{w^2}^+$), the effect of spatial averaging for the large FOV is clearly visible much further away from the wall (Figure 6(c)). Since there is limited experimental data at the Re_τ considered in this study, comparisons are made with an empirical formulation (−−), obtained from a structural model of the boundary layer. This model has been validated against single point experimental measurements carried out at Reynolds numbers up to $Re_\tau = \mathcal{O}(10^5)$ and is detailed in Kunkel and Marusic.[34] The larger influence of spatial averaging in $\overline{w^2}^+$ can be attributed to the smaller scales of the wall-normal fluctuations. This is supported by the fact that the high-mag FOV shows much better agreement with the $\overline{w^2}^+$ profile of the model, due to its higher spatial resolution. We note a sharp change in $\overline{w^2}^+$ at the transition point between the bottom and top cameras of the large FOV, which is primarily caused by the variation in spatial

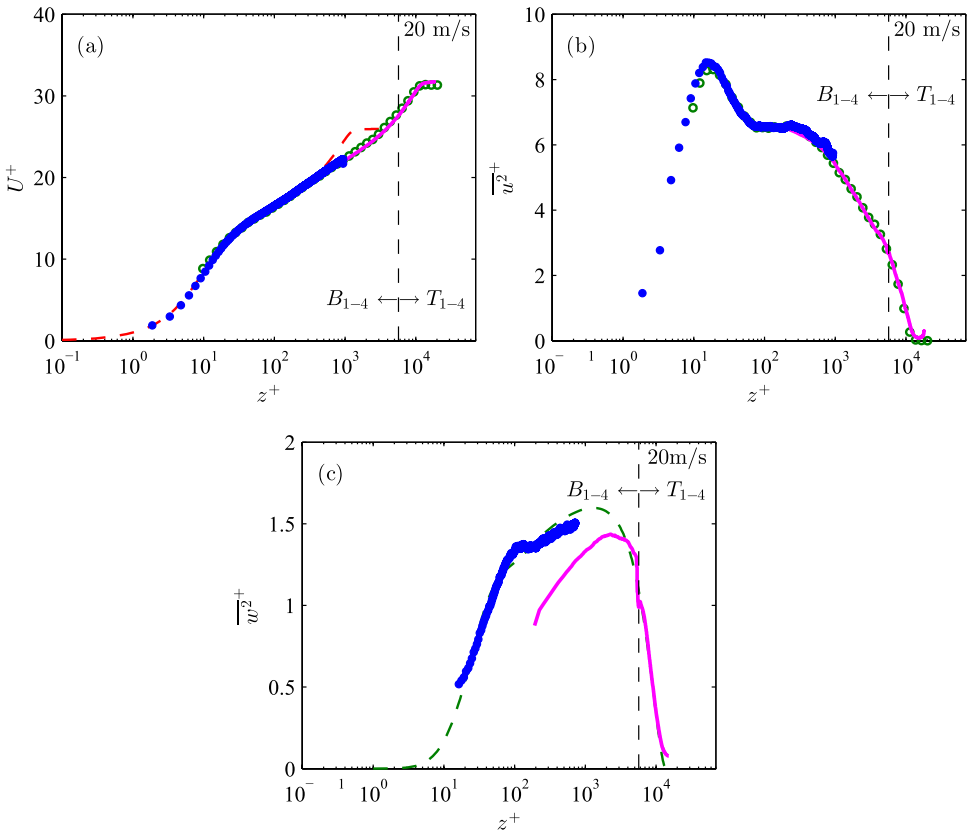

FIG. 7. Comparison of planar PIV results with results from hot-wire anemometry experiments and empirical formulations at $Re_\tau \approx 14\,500$ for flow statistics (a) U^+, (b) $\overline{u^2}^+$, and (c) $\overline{w^2}^+$. Symbols are defined in Figure 6.

resolution between the two magnification levels (40 and 65 viscous units at $Re_\tau \approx 8000$ for the bottom and top cameras, respectively). To validate that spatial resolution is indeed the cause of this sharp change, a comparison is made between filtered wall-normal turbulence intensity ($\overline{w_f^2}^+$) profiles from a DNS dataset;[9] one filtered at $39 \times 39 \times 11$ (resolution of bottom cameras) viscous units and the other at $64 \times 64 \times 11$ (resolution of top cameras) viscous units. Thereafter, a comparison is made at $z/\delta \approx 0.35$, where the transition from the bottom to top cameras occur. Results, show a step change of approximately 15% in $\overline{w_f^2}^+$ caused by this change in resolution which is comparable to that observed in the experimental data (see Figure 6(c)).

Figure 7 shows velocity statistics (U^+, $\overline{u^2}^+$, and $\overline{w^2}^+$ profiles) at $Re_\tau \approx 14\,500$. Again good agreement of the mean velocity profiles with the hot-wire measurement is seen to within a few wall units ($1 - 3$). It should be noted that the interrogation window size is halved (16×16 pixels) for the large FOV in an attempt to match the spatial attenuation of flow statistics, therefore similar agreement in $\overline{u^2}^+$ is observed. However, as a caution it is noted that this agreement may be attributed to noise in the PIV velocity field associated with using smaller interrogation window sizes, which may be negating spatial attenuation. Nevertheless, encouraging agreement is observed in both Figures 6 and 7 for the flow statistics considered. Flow statistics (U^+, $\overline{u^2}^+$, and $\overline{w^2}^+$) at $Re_\tau \approx 19\,500$ also show similar collapse but with increased spatial attenuation as one would expect at higher Re_τ and are not reproduced here for brevity.

B. Wall shear stress

The measurement of the wall shear stress (and hence U_τ), particularly instantaneous wall shear stress over any reasonable area, has always been challenging. For a review of techniques to measure

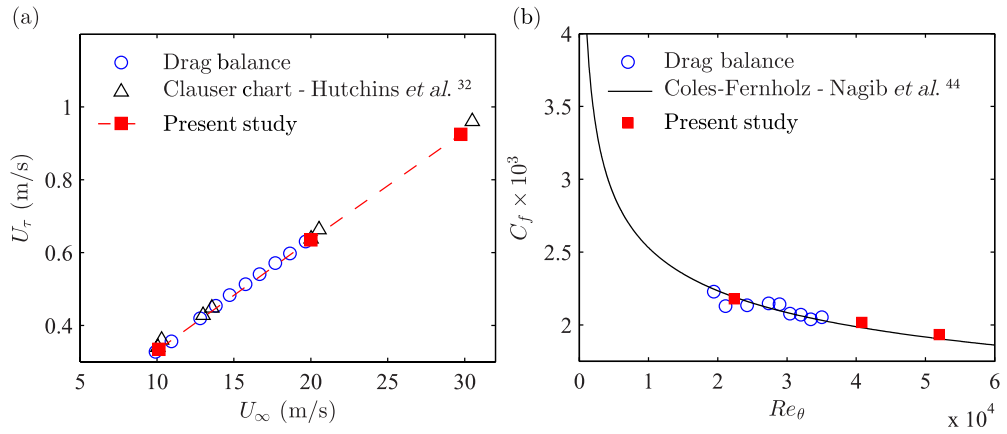

FIG. 8. (a) Comparison of U_τ with U_∞ from the high-mag PIV experiment compared with prior results from a drag-balance and Clauser chart results of Hutchins *et al.*[32] in the same facility at the same streamwise position. (b) Comparison of C_f against the Coles-Fernholz empirical relation for C_f with Re_θ,[44] and prior results from a drag-balance in the same facility.

wall shear stress, readers are directed to Winter[37] and Naughton and Sheplak.[38] Currently, oil film interferometry is the most common and reliable technique to measure the mean (time-averaged) wall shear stress with an accuracy of $\pm$ 1%–2%. However, this technique cannot measure instantaneous fluctuations and is limited to certain geometries[39] (cannot be applied to rough surfaces). More recently, modest progress has been made with alternate techniques (see Gnanamanickam *et al.*,[40] Große and Schröder,[41] Amili and Soria[42]) to measure instantaneous wall shear stress, albeit at low Re_τ. However, if one can measure the velocity field within the viscous sublayer, the wall shear stress of a smooth wall can be computed directly. This becomes challenging at high Re_τ as the thickness of the sublayer typically decreases with increasing Reynolds number for a given facility.

Qualitatively, it is evident from Figure 4 that the present measurements provide velocity vectors within the viscous sublayer. This enables the computation of the instantaneous wall shear stress (τ_w) and the instantaneous friction velocity ($\widetilde{U}_\tau$) directly using

$$\widetilde{U}_\tau = \sqrt{\frac{\tau_w}{\rho}} = \sqrt{\nu \frac{\partial \widetilde{U}}{\partial z}}. \tag{4}$$

The instantaneous wall shear stress is estimated using the velocity field at a wall normal location of $z^+ \approx$ 4–5 viscous units. A linear velocity distribution is then assumed in the sublayer to calculate τ_w. This linear variation is an assumption and instantaneous velocity profiles from DNS, albeit at lower Re_τ, show a certain degree of nonlinearity within the sublayer. One such example is a study by Große and Schröder[43] which states that the standard deviation of the velocity profile (within the viscous sublayer) from a linear distribution is 0.06. Nevertheless, in the absence of sufficient data in the region $0 < z^+ < 3$, we must rely on this assumed linearity in order to extract the fluctuating shear stress from the acquired velocity fields.

Figure 8(a) shows the variation in U_τ with freestream velocity U_∞ compared with prior skin friction measurements obtained from a drag balance facility and Hutchins *et al.*[32] (Clauser chart method with $\kappa = 0.41$ and $A = 5$). Results indicate good agreement of U_τ between the three independent measurements (and techniques) up to 30 ms^{-1}($Re_\tau \approx 19\,500$). Similarly, Figure 8(b) compares the skin-friction coefficient C_f against measurements from a drag balance facility, and the Coles-Fernholz empirical relation defined as

$$C_f = 2[1/\kappa \ \ln(Re_\theta) + C]^{-2}, \tag{5}$$

where $\kappa = 0.384$ and $C = 4.127$ as given by Nagib, Chauhan, and Monkewitz.[44] Good agreement of C_f is observed between the datasets from this study and the empirical formulation.

The probability distribution of the wall shear stress fluctuations can also be calculated. The pdf of the wall shear stress fluctuations at the three Re_τ under consideration are presented

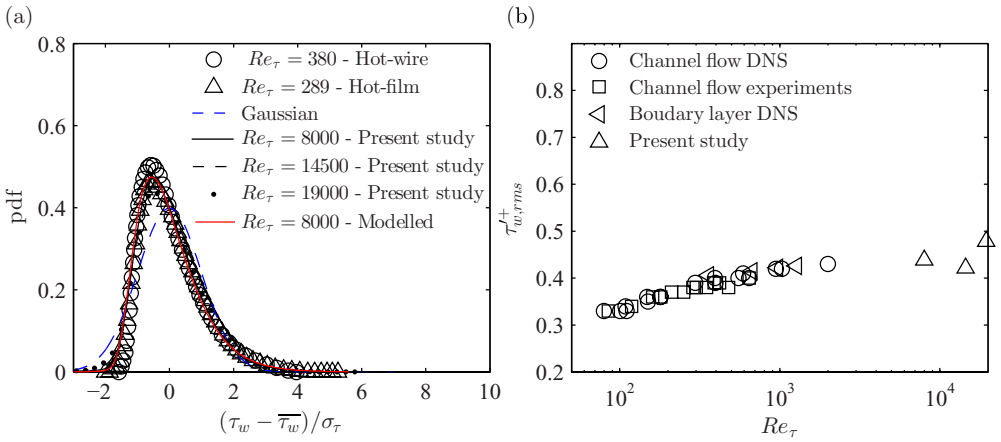

FIG. 9. (a) Probability density function of wall shear stress fluctuations, ○ shows hot-wire data at $Re_\tau = 380$ from Khoo, Chew, and Teo,[45] △ shows hot-film data at $Re_\tau = 289$ from Sreenivasan and Antonia.[46] Blue dashed line shows a Gaussian distribution with $\sigma = 1$, and the solid, dashed, and dotted lines represent datasets from present study. The solid red line represents a modelled shear stress distribution.[47] (b) Variation in the turbulent intensity of the wall shear stress fluctuations ($\tau'^{+}_{w,rms}$), ○ channel flow DNS datasets,[9,48] □ channel flow experimental datasets,[45] ◁ boundary layer DNS datasets,[11] and △ represent datasets from present study.

in Figure 9(a). The plotted pdf is of the fluctuating wall shear stress normalised by its standard deviation in the manner of Hu, Morfey, and Sandham[49] and Keirsbulck, Labraga, and Gad-el Hak.[50] Also included are existing measurements (shown in △ and ○) that are summarised in Keirsbulck, Labraga, and Gad-el Hak,[50] and a Gaussian distribution for reference. It is noted that the bulk of these measurements are at significantly lower Re_τ (by an order of magnitude) than those considered in this study, although good agreement is observed between them. The pdf's shown in Figure 9(a) appear to be invariant with Reynolds number, however, this observation is not conclusive, since factors such as the spatial resolution of each measurement (or technique) and their associated uncertainties would need to be considered before a conclusion is reached. Furthermore, since limited experimental data are available at the Re_τ considered in this study, the wall shear stress pdf at $Re_\tau = 8000$, computed using the model presented by Mathis *et al.*[47] is also included in Figure 9. Comparisons to the predicted pdf from this model shows good agreement with datasets from this study.

Figure 9(b) shows the variation in the turbulent intensity of the wall shear stress fluctuations ($\tau'^{+}_{w,rms}$) as a function of Re_τ. The turbulent intensity of a collection of DNS datasets is presented in the range $Re_\tau \approx 100 - 1000$ for both channel flows and boundary layers. The present study extends the range of Re_τ considered by an order of magnitude to $Re_\tau = 19\,500$, and appears to follow the existing trend of the datasets at lower Re_τ. It should be noted that in spite of the unprecedented spatial resolution of the presented PIV measurements, the data presented are spatially averaged, more so at the higher Re_τ and may underpredict $\tau'^{+}_{w,rms}$. While the results discussed in this section are encouraging, a better estimate of the wall shear stress could be attained by attempting to obtain estimates of the velocity closer to the wall by using particle tracking techniques,[26,51] or by the acquisition of a dataset that is optimised for a high magnification level only.

C. Conditional analysis

The instantaneous velocity fields measured in this study have a spatial range of up to 2δ while resolving the smaller scales close to the Kolmogorov scale η, providing an available scale range of $2\delta/\eta \approx 10^3$. Additionally, the high-mag FOV provides instantaneous velocity data within the viscous sublayer, which are used to compute the instantaneous wall shear stress as detailed previously in Sec. IV B. The simultaneous use of the large and high-mag FOVs allows for the study of near-wall events and any links between these near-wall events and the much larger features that populate the

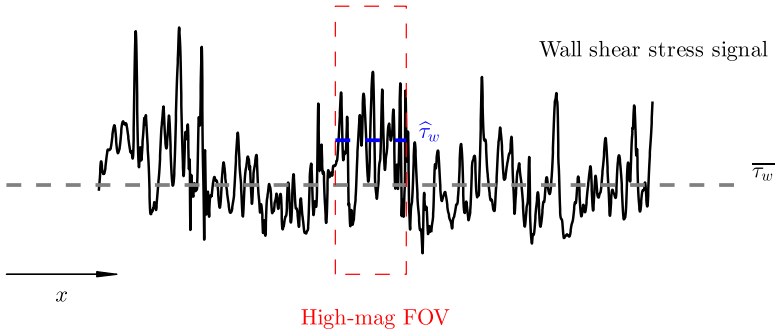

FIG. 10. Schematic showing a sample wall shear stress signal evolving with x. The dashed red box corresponds to the streamwise length of the high-mag FOV. The corresponding local mean $\widehat{\tau_w}$ is shown by a blue dashed line and the global mean ($\overline{\tau_w}$) is represented by the grey dashed line.

log and wake regions. Exploring the connection between near-wall events and the structures in the log region has proven fruitful in the development of models. For example, the predictive model described in Marusic, Mathis, and Hutchins[52] is able to reconstruct a fluctuating streamwise velocity signal accurately in the near-wall region, given only the large-scale streamwise velocity signal in the log-region. The work of Mathis *et al.*[47] extends this model to estimate wall shear stress fluctuations.

Recent work by Hutchins *et al.*[53] employed surface heat transfer skin friction gauges to study such interactions. However, they highlighted the limitations of these sensors to resolve high frequency fluctuations in shear stress. This drawback is overcome in the present study as the high-mag FOV resolves much higher frequencies in wall shear stress fluctuations at high Re_τ. Furthermore, most prior studies employed single-point measurement techniques, and required the use of Taylor's hypothesis to obtain spatial variations. Conversely, here we obtain instantaneous spatial information, thus not invoking Taylor's hypothesis.

The analysis to be performed provides an average structure within the boundary layer, and hence a visual and quantitative representation of the overlaying features. Furthermore, it serves as a demonstration of the simultaneous use of the high-mag and large FOV, to study the amplitude modulation of small-scale events near the wall by the larger features in the log region and beyond. Using well resolved shear stress fluctuations, a conditional analysis is performed based on the variance of the skin friction signal. It is to be noted that this analysis differs from Hutchins *et al.*,[53] where a conditional average was produced based on a large-scale skin friction event sensed at the wall. A low variance shear stress event (quiescent shear stress fluctuation region) is defined as

$$u(x,z)|_l = \langle u(x,z) \,|\, \widehat{\tau_w^{*2}} < t_l \rangle, \tag{6}$$

where $u(x, z)$ denotes the fluctuating velocity component, and τ_w^* corresponds to the fluctuating shear stress about a local mean $\widehat{\tau_w}$ (illustrated in Figure 10) . $\widehat{\tau_w}$ is defined as the average wall shear stress over the streamwise length of the high mag FOV (500 viscous units at $Re_\tau = 8000$). Therefore, the subtraction of this local mean is equivalent to filtering the large-scale fluctuations from the instantaneous wall shear stress signal leaving only fluctuations that are smaller than the streamwise length of the high mag FOV. Thus, $\widehat{\tau_w^{*2}}$ can be viewed as the magnitude of the small scale variance of the wall shear stress fluctuations. The angle brackets denote the ensemble average of the detected events. t_l corresponds to the threshold employed to isolate 20% of the lowest $\widehat{\tau_w^{*2}}$ events (frames from the high-mag FOV) from the total dataset.

Figure 11(b) shows iso-contours of the streamwise velocity fluctuations $u|_l$ obtained from the high-mag FOV, when conditioned on low variance shear stress events (Eq. (6)). An inclined, forward leaning, low speed structure is observed extending across the entire high-mag FOV. In fact, this structure extends well into the large FOV (Figure 11(a)). The large FOV, which spans 2δ in the streamwise direction, suggests that on average low variance shear stress fluctuations events at the wall are associated with a large-scale structure that has a streamwise length of $\mathcal{O}(\delta)$. This structure is inclined at an angle of approximately 14° to the wall, which is consistent with inclination angles

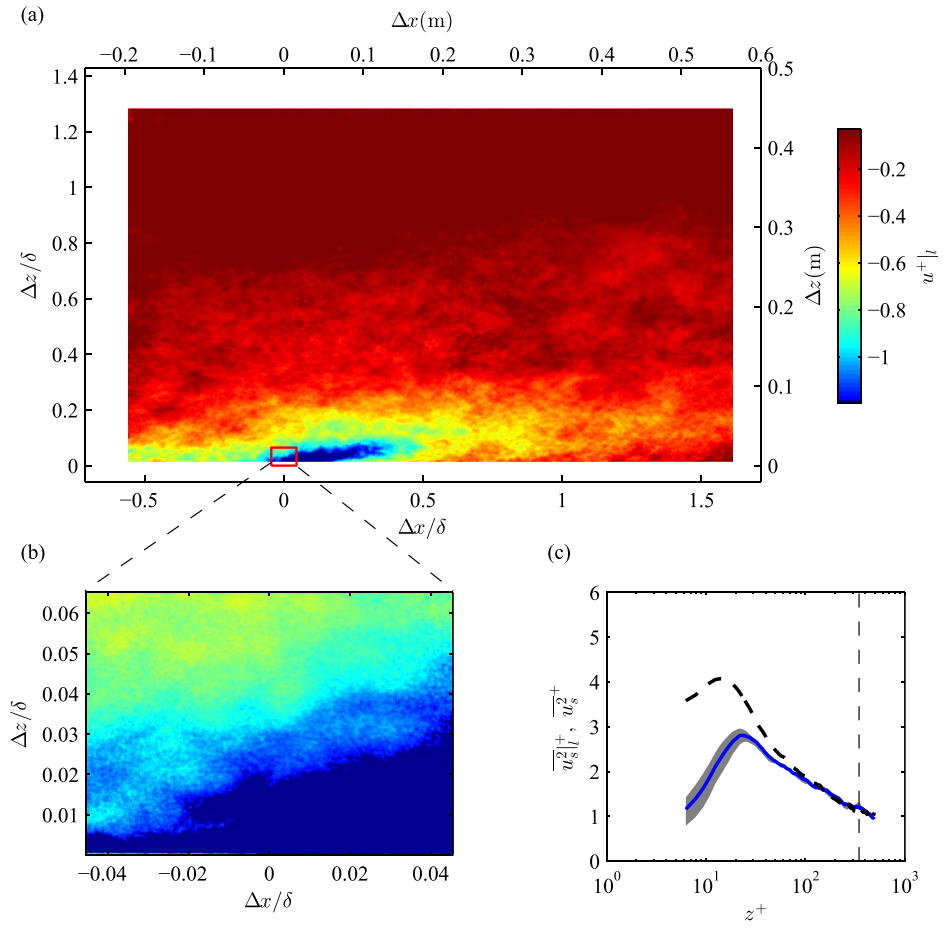

FIG. 11. (a) Iso-contours of conditioned streamwise velocity fluctuations ($u^+|_l$) across the large FOV, conditionally averaged over low energetic shear stress fluctuations events (Eq. (6) at $Re_\tau \approx 8000$). (b) Region in (a) as seen with the high-mag FOV. (c) Turbulence intensity profiles of $\overline{u_s^2}|_l$ (conditioned small-scale variance) and $\overline{u_s^2}$ (unconditional small-scale variance) across the high-mag FOV shown by a solid (–) and dashed lines (−−), respectively. Note that the shaded region encapsulates $\overline{u_s^2}|_l$ computed at two threshold levels (t_1) to isolate 10% and 30% of the total dataset. The vertical dashed line corresponds to $z^+ = \sqrt{15Re_\tau}$.

reported in cross-correlations between τ_w and $\widetilde{U}$ in the logarithmic region of boundary layers.[54] Conversely, when the shear stress is highly turbulent we observe a similar large-scale structure but with an opposite sign (large high speed event), which is not shown here for brevity. These results demonstrate using well resolved shear stress fluctuations, the modulating influence of larger features in the log region on shear stress fluctuations. Prior studies[53] have qualitatively shown such phenomena by performing a conditional average of small scale velocity fluctuations conditioned on a large-scale shear stress fluctuation at the wall. The present results definitively show that increased (or reduced) small-scale variance in shear stress fluctuations is indeed associated with the passage of very large-scale positive (or negative) velocity fluctuations. This analysis offers a good demonstration of the capabilities of this high Reynolds number nested PIV measurement technique. The modulation effect can only be observed at sufficiently high Reynolds numbers where scale separation is possible between large and small scales. In addition, we can only sensibly analyse this modulation if we have a simultaneous view of the very large scale events and the small scale fluctuations near the wall, both of which are provided by this unique measurement.

Figure 11(c) shows the streamwise small-scale velocity variance for quiescent shear stress events. The conditioned small-scale variance is given by $\overline{u_s^2}|_l$ (—), and the unconditioned small-scale variance is denoted by $\overline{u_s^2}$ (−−). The small scale variance (denoted by subscript s) is obtained using

the local mean computed with a streamwise length of the high-mag FOV ($\sim 0.06\delta$), thus isolating length scales less than $\sim 0.06\delta$. Results show reduced small-scale variance (i.e., $\overline{u_s^2}|_l / \overline{u_s^2} < 1$) across the entire wall-normal span of the high-mag FOV. We note that beyond (above) the scope of the high-mag FOV a marginal increase ($\sim 5\%$) in the small-scale variance is observed with a cross over in close proximity to $z^+ \approx \sqrt{15 Re_\tau}$, similar to that suggested by Mathis, Hutchins, and Marusic.[55]

The effect of the threshold level (t_1) on $\overline{u_s^2}|_l$ is exhibited in Figure 11(c) by the shaded region, which corresponds to 10% and 30% of the lowest $\widehat{\tau_w^{*2}}$ events (frames from the high-mag FOV) from the total dataset. Even though there is a slight shift in the measured distributions, the overall trend is the same, leading to the same conclusions drawn in this analysis. In summary, these results illustrate the scope of the present dataset in probing links between near wall events associated with wall shear stress and those in the log region and beyond.

V. CONCLUSIONS

This study details and analyses a unique multi-camera, multi-resolution PIV configuration, to carry out velocity measurements in a streamwise wall-normal plane at high Re_τ. A large FOV coupled with a simultaneous high magnification inset, captures the large range of length scales prevalent at high Re_τ, providing almost an order of magnitude increase in dynamic spatial range relative to prior measurements.[15] The velocity fields measured using the present configuration compares well with prior hot-wire anemometry results, providing some validation of the accuracy of the current setup.

The inclusion of the high magnification inset (high-mag FOV) enables us to resolve the near wall region up to a few wall units ($1 - 3$) from the wall. Consequentially, the high-mag FOV enables us to directly compute the mean friction velocity (and wall shear stress), which is typically found using empirical fits or oil film interferometry. The mean friction velocity thus calculated compares well with both independent measurements and historical correlations. Furthermore, the instantaneous wall shear stress is also computed, and good agreement with existing literature is shown for wall shear stress statistics. A closer estimate of these statistics, which are associated with the wall shear stress, may be attained by attempting to get closer to the near wall region, perhaps using particle tracking techniques as suggested by Cierpka, Scharnowski, and Kähler,[26] Kähler, Scharnowski, and Cierpka,[51] or by the acquisition of a dataset that is optimised for a high magnification level only.

The simultaneous use of the large and high-mag FOV is shown to be an ideal candidate to perform conditional statistics between small-scale features observed in the near-wall region and the overlying larger structures in the outer regions, which would be on the order of δ (and observable simultaneously in the large FOV). Using well resolved wall shear stress signals the present results definitively show that increased (or reduced) small-scale variance in wall shear stress fluctuations are indeed associated with the passage of very large-scale positive or negative velocity fluctuations.

ACKNOWLEDGMENTS

The authors gratefully acknowledge support from the Australian Research Council.

[1] I. Marusic, B. J. McKeon, P. A. Monkewitz, H. M. Nagib, A. J. Smits, and K. R. Sreenivasan, "Wall-bounded turbulent flows at high Reynolds numbers: Recent advances and key issues," Phys. Fluids **22**, 065103 (2010).
[2] J. C. Klewicki, "Reynolds number dependence, scaling, and dynamics of turbulent boundary layers," J. Fluids Eng. **132**, 094001 (2010).
[3] J. Jiménez, "Cascades in wall-bounded turbulence," Annu. Rev. Fluid Mech. **44**, 27–45 (2012).
[4] A. J. Smits, B. J. McKeon, and I. Marusic, "High-Reynolds number wall turbulence," Annu. Rev. Fluid Mech. **43**, 353–375 (2011).
[5] I. Marusic, R. Mathis, and N. Hutchins, "High Reynolds number effects in wall turbulence," J. Heat Fluid Flow **31**, 418–428 (2010).
[6] I. Marusic and R. J. Adrian, "The eddies and scales of wall turbulence," *Ten Chapters in Turbulence* (Cambridge University Press, 2012).
[7] S. Herpin, M. Stanislas, J. M. Foucaut, and S. Coudert, "Influence of the Reynolds number on the vortical structures in the logarithmic region of turbulent boundary layers," J. Fluid Mech. **716**, 5–50 (2013).
[8] N. Hutchins and I. Marusic, "Evidence of very long meandering features in the logarithmic region of turbulent boundary layers," J. Fluid Mech. **579**, 1–28 (2007).

[9] S. Hoyas and J. Jimenez, "Scaling of the velocity fluctuations in turbulent channels up to $Re_\tau = 2003$," Phys. Fluids **18**, 011702 (2006).
[10] S. Pirozzoli and M. Bernardini, "Probing high-Reynolds-number effects in numerical boundary layers," Phys. Fluids **25**, 021704 (2013).
[11] P. Schlatter and R. Örlü, "Assessment of direct numerical simulation data of turbulent boundary layers," J. Fluid Mech. **659**, 116–126 (2010).
[12] M. Raffel, C. E. Willert, S. T. Wereley, and J. Kompenhans, *Particle Image Velocimetry: A Practical Guide* (Springer, Berlin, 2007).
[13] R. J. Adrian and J. Westerweel, *Particle Image Velcimetry* (Cambridge University Press, 2011).
[14] R. J. Adrian, C. D. Meinhart, and C. D. Tomkins, "Vortex organization in the outer region of the turbulent boundary layer," J. Fluid Mech. **422**, 1–54 (2000).
[15] J. Westerweel, G. E. Elsinga, and R. J. Adrian, "Particle image velocimetry for complex and turbulent flows," Annu. Rev. Fluid Mech. **45**, 409–436 (2013).
[16] C. D. Tomkins and R. J. Adrian, "Spanwise structure and scale growth in turbulent boundary layers," J. Fluid Mech. **490**, 37–74 (2003).
[17] N. Hutchins, W. T. Hambleton, and I. Marusic, "Inclined cross-stream stereo particle image velocimetry measurements in turbulent boundary layers," J. Fluid Mech. **541**, 21–54 (2005).
[18] J. Carlier and M. Stanislas, "Experimental study of eddy structures in a turbulent boundary layer using particle image velocimetry," J. Fluid Mech. **535**, 143–188 (2005).
[19] W. T. Hambleton, N. Hutchins, and I. Marusic, "Simultaneous orthogonal-plane particle image velocimetry measurements in a turbulent boundary layer," J. Fluid Mech. **560**, 53–64 (2006).
[20] J. Lin, J. P. Laval, J. M. Foucaut, and M. Stanislas, "Quantitative characterisation of coherent structures in the buffer layer of near-wall turbulence. Part 1: Streaks," Exp. Fluids **45**, 999–1013 (2008).
[21] S. Herpin, C. Y. Wong, M. Stanislas, and J. Soria, "Stereoscopic PIV measurements of a turbulent boundary layer with a large spatial dynamic range," Exp. Fluids **45**, 745–763 (2008).
[22] A. Schröder, R. Geisler, K. Staack, G. E. Elsinga, F. Scarano, B. Wieneke, A. Henning, C. Poelma, and J. Westerweel, "Eulerian and Lagrangian views of a turbulent boundary layer flow using time-resolved tomographic PIV," Exp. Fluids **50**, 1071–1091 (2011).
[23] G. E. Elsinga, D. J. Kuik, B. W. van Oudheusden, and F. Scarano, "Investigation of the three-dimensional coherent structures in a turbulent boundary layer with tomographic-PIV," AIAA Paper 2007-1305, 2007.
[24] G. E. Elsinga, R. J. Adrian, B. W. Van Oudheusden, and F. Scarano, "Three-dimensional vortex organization in a high-Reynolds-number supersonic turbulent boundary layer," J. Fluid Mech. **644**, 35–60 (2010).
[25] T. H. Clark, "Measurement of three-dimensional coherent fluid structure in high Reynolds number turbulent boundary layers," Ph.D. thesis, Trinity Hall, Cambridge, 2012.
[26] C. Cierpka, S. Scharnowski, and C. J. Kähler, "Parallax correction for precise near-wall flow investigations using particle imaging," Appl. Opt. **52**, 2923–2931 (2013).
[27] T. B. Nickels, I. Marusic, S. Hafez, and M. S. Chong, "Evidence of the k-1 law in a high-Reynolds-number turbulent boundary layer," Phys. Rev. Lett. **95**, 074501 (2005).
[28] C. M. de Silva, R. Baidya, M. Khashehchi, and I. Marusic, "Assessment of tomographic PIV in wall-bounded turbulence using direct numerical simulation data," Exp. Fluids **52**, 425–440 (2012).
[29] C. M. de Silva, J. Philip, K. Chauhan, C. Meneveau, and I. Marusic, "Multiscale geometry and scaling of the turbulent-nonturbulent interface in high Reynolds number boundary layers," Phys. Rev. Lett. **111**, 044501 (2013).
[30] G. I. Roth and J. Katz, "Five techniques for increasing the speed and accuracy of PIV interrogation," Meas. Sci. Technol. **12**, 238–245 (2001).
[31] R. J. Adrian, "Dynamic ranges of velocity and spatial resolution of particle image velocimetry," Meas. Sci. Technol. **8**, 1393 (1997).
[32] N. Hutchins, T. B. Nickels, I. Marusic, and M. S. Chong, "Hot-wire spatial resolution issues in wall-bounded turbulence," J. Fluid Mech. **635**, 103–136 (2009).
[33] V. Kulandaivelu, "Evolution of zero pressure gradient turbulent boundary layers from different initial conditions," Ph.D. thesis, The University of Melbourne, 2012.
[34] G. J. Kunkel and I. Marusic, "Study of the near-wall-turbulent region of the high-Reynolds number boundary layer using an atmospheric flow," J. Fluid Mech. **548**, 375–402 (2006).
[35] J. P. Monty, N. Hutchins, H. C. H. Ng, I. Marusic, and M. S. Chong, "A comparison of turbulent pipe, channel and boundary layer flows," J. Fluid Mech. **632**, 431 (2009).
[36] C. Atkinson, N. A. Buchmann, O. Amili, and J. Soria, "On the appropriate filtering of PIV measurements of turbulent shear flows," Exp. Fluids **55**, 1654 (2013).
[37] K. G. Winter, "An outline of the techniques available for the measurement of skin friction in turbulent boundary layers," Prog. Aero. Sci. **18**, 1–57 (1979).
[38] J. W. Naughton and M. Sheplak, "Modern developments in shear-stress measurement," Prog. Aero. Sci. **38**, 515–570 (2002).
[39] P. A. Monkewitz, K. A. Chauhan, and H. M. Nagib, "Self-consistent high-Reynolds-number asymptotics for zero-pressure-gradient turbulent boundary layers," Phys. Fluids **19**, 115101 (2007).
[40] E. P. Gnanamanickam, B. Nottebrock, S. Große, J. P. Sullivan, and W. Schröder, "Measurement of turbulent wall shear-stress using micro-pillars," Meas. Sci. Technol. **24**, 124002 (2013).
[41] S. Große and W. Schröder, "Wall-shear stress patterns of coherent structures in turbulent duct flow," J. Fluid Mech. **633**, 147–58 (2009).
[42] O. Amili and J. Soria, "A film-based wall shear stress sensor for wall-bounded turbulent flows," Exp. Fluids **51**, 137–147 (2011).

[43] S. Große and W. Schröder, "The micro-pillar shear-stress sensor MPS3 for turbulent flow," Sensors **9**, 2222–2251 (2009).
[44] H. M. Nagib, K. A. Chauhan, and P. A. Monkewitz, "Approach to an asymptotic state for zero pressure gradient turbulent boundary layers," Philos. Trans. R. Soc. London, Ser. A **365**, 755–770 (2007).
[45] B. C. Khoo, Y. T. Chew, and C. J. Teo, "On near-wall hot-wire measurements," Exp. Fluids **29**, 448–460 (2000).
[46] K. R. Sreenivasan and R. A. Antonia, "Properties of wall shear stress fluctuations in a turbulent duct flow," Trans. ASME **44**, 389–395 (1977).
[47] R. Mathis, I. Marusic, S. I. Chernyshenko, and N. Hutchins, "Estimating wall-shear-stress fluctuations given an outer region input," J. Fluid Mech. **715**, 163–180 (2013).
[48] J. C. del Alamo, J. Jimenez, P. Zandonade, and R. D. Moser, "Scaling of the energy spectra of turbulent channels," J. Fluid Mech. **500**, 135–144 (2004).
[49] Z. Hu, C. L. Morfey, and N. D. Sandham, "Wall pressure and shear stress spectra from direct simulations of channel flow," AIAA J. **44**, 1541–1549 (2006).
[50] L. Keirsbulck, L. Labraga, and M. Gad-el Hak, "Statistical properties of wall shear stress fluctuations in turbulent channel flows," J. Heat Fluid Flow **37**, 1–8 (2012).
[51] C. J. Kähler, S. Scharnowski, and C. Cierpka, "On the uncertainty of digital PIV and PTV near walls," Exp. Fluids **52**, 1641–1656 (2012).
[52] I. Marusic, R. Mathis, and N. Hutchins, "Predictive model for wall-bounded turbulent flow," Science **329**, 193–196 (2010).
[53] N. Hutchins, J. P. Monty, B. Ganapathisubramani, H. C. H. Ng, and I. Marusic, "Three-dimensional conditional structure of a high-Reynolds number turbulent boundary layer," J. Fluid Mech. **673**, 255–285 (2011).
[54] I. Marusic and W. D. Heuer, "Reynolds number invariance of the structure inclination angle in wall turbulence," Phys. Rev. Lett. **99**, 114504 (2007).
[55] R. Mathis, N. Hutchins, and I. Marusic, "Large-scale amplitude modulation of the small-scale structures in turbulent boundary layers," J. Fluid Mech. **628**, 311–337 (2009).